



## 3D estimation of soft biological tissue deformation from radio-frequency ultrasound volume acquisitions

Jean-François Deprez<sup>a,\*</sup>, Elisabeth Brusseau<sup>a</sup>, Cédric Schmitt<sup>b</sup>, Guy Cloutier<sup>b</sup>, Olivier Basset<sup>a</sup>

<sup>a</sup>CREATIS, Université de Lyon, INSA de Lyon, Université Lyon 1, CNRS UMR 5220, INSERM U 630, Bâtiment Blaise Pascal, 7 avenue Jean Capelle, F-69621 Villeurbanne, France

<sup>b</sup>Laboratoire de Biorhéologie et d'Ultrasonographie Médicale (LBUM), Centre Hospitalier de l'Université de Montréal, Hôpital Notre-Dame, Pavillon J.A de Seve (Y-1619), 2099 Alexandre de Seve, Montréal, Québec, Canada H2L 2W5

### ARTICLE INFO

#### Article history:

Received 18 October 2007

Received in revised form 1 July 2008

Accepted 14 July 2008

Available online 30 July 2008

#### Keywords:

Elastography  
Image processing  
Strain estimation  
Ultrasound

### ABSTRACT

The current research and development of 2D (matrix-shaped) transducer arrays to acquire 3D ultrasound data sets provides new insights into medical ultrasound applications and in particular into elastography.

Until very recently, tissue strain estimation techniques commonly used in elastography were mainly 1D or 2D methods. In this paper, a 3D technique estimating biological soft tissue deformation under load from ultrasound radiofrequency volume acquisitions is introduced. This method locally computes axial strains, while considering lateral and elevational motions. Optimal deformation parameters are estimated as those maximizing a similarity criterion, defined as the normalized correlation coefficient, between an initial region and its deformed version, when the latter is compensated for according to these parameters.

The performance of our algorithm was assessed with numerical data reproducing the configuration of breast cancer, as well as a physical phantom mimicking a pressure ulcer. Simulation results show that the estimated strain fields are very close to the theoretical values, perfectly discriminating between the harder lesion and the surrounding medium. Experimental strain images of the physical phantom demonstrated the different structures of the medium, even though they are not all detectable on the ultrasound scans.

Finally, both simulated and experimental results demonstrate the ability of our algorithm to provide good-quality elastograms, even in the conditions of significant out-of-plane motion.

© 2008 Elsevier B.V. All rights reserved.

### 1. Introduction

Pathological processes very often induce changes in soft tissue stiffness (Anderson and Kissane, 1953; Lendon et al., 1991; Lee et al., 1991; Ariel and Cleary, 1987), which is why physicians first use palpation to detect tumors, especially in the breast or prostate. However, this examination is restricted to shallow tumors and pathologies at a late stage. These limitations motivated a new imaging technique termed ultrasound elastography. This technique provides information on the local elastic properties of a tissue by visualizing its deformation behavior in response to an external load. Depending on the nature of the mechanical excitation applied to the tissues, either a static load or a vibration, ultrasound elastography techniques fall into two categories: static elastography and sono-elastography, respectively. This paper investigates strain estimation in static elastography.

Ultrasound elastography is inspired by a basic rule of mechanics: subjected to a given stress, soft areas will deform more than

harder ones. In practical terms, ultrasound radiofrequency (RF) images are acquired from the tissue under investigation in both rest and compressed states (also termed pre- and post-compression states). Tissue internal deformations are then locally estimated. Ultrasound data are divided into many overlapping regions of interest (ROI) and for each ROI, stress-induced changes within the signals are analyzed to generate a map of the local strain.

Accurately estimating the strain remains fundamental in elastography since the clinician's diagnosis, as well as the quality of mechanical parameter reconstruction, is directly related to these estimations.

Until recently, mainly one-dimensional (1D) methods had been developed. They provide a map of the axial component of the deformation, along the ultrasound beam's propagation axis. The first technique, originally developed by Ophir et al. (1991), is based on a time-delay estimation. It assumes that with compression, the tissue locally experiences simple axial translations. Within the RF signal, this results in time-delays for the corresponding acoustical footprints. Cross-correlation is therefore applied to short segments of pairs of pre- and post-compression RF A-lines, and the location

\* Corresponding author. Tel.: +33 4 72 43 62 54; fax: +33 4 72 43 85 26.  
E-mail address: [deprez@creatis.insa-lyon.fr](mailto:deprez@creatis.insa-lyon.fr) (J.-F. Deprez).

of the peak of the correlation function estimates this shift. Strain is then calculated as the gradient of the displacement. Since these time-delay techniques do not take into account the signal shape variation caused by the compression, they rapidly fail with high strains. Moreover, the gradient function is a very noise-sensitive operator. To overcome these limitations, a second category of 1D methods were proposed, namely the local scaling factor estimation techniques (Alam et al., 1998; Bilgen, 1999; Brusseau et al., 2000). With these techniques, the post-compression signal is locally assumed to be an axially shifted and compressed replica of the initial signal. Since this hypothesis is closer to reality than the previous one, it improves the robustness of the estimation.

Unfortunately, these techniques often lead to insufficiently accurate results, because these estimators remain one-dimensional, whereas the tissue motion that occurs during the load is three-dimensional. As biological media can reasonably be considered as incompressible, the axial compression applied to the tissues also yields to lateral and elevational expansions. Tissue acoustical scatterers therefore experience 3D displacements. One-dimensional techniques only consider the transformation of the acoustical footprint of the pre-compression signal due to the axial displacement of the scatterers, whereas lateral and out-of-plane motions of the scatterers are also responsible for the acoustical signature modification. This is a major source of decorrelation between pre- and post-compression data.

To transcend these limitations and approach 3D motion, 2D estimators were first developed. Two-dimensional techniques were also motivated by the fact that most ultrasound devices currently in clinical use only provide 2D images. Several approaches can be mentioned.

- (i) The conventional technique, taking inspiration from block-matching, is the 2D speckle tracking method (O'Donnell et al., 1994). Two-dimensional local displacement is modeled as a translation in both axial and lateral directions. But the enhancement of the accuracy is limited, since this type of technique ignores the signal shape variation. According to Pellot-Barakat et al. (2004), data alone may be insufficient to solve ambiguities due to loss of echo coherence. Integrating *a priori* knowledge may therefore be necessary. The displacement field is estimated by minimizing an energy function that includes constraints of echo amplitude conservation and displacement field continuity. However, this approach only considers constant signal shifts (not scaling) and the field continuity parameter may excessively smoothen the boundaries. Konofagou and Ophir (1998) proposed both global stretching and lateral weighted interpolation of the post-compression signals, prior to strain estimation. The scaled replica of each 1D acoustical footprint is then searched in the axial and lateral directions. Nevertheless, two limits should be pointed out: first, global stretching is not suitable because it does not fit the local signal changes. Moreover, the lateral resolution is limited by the interpolation rate chosen.
- (ii) Companding, developed by Chaturvedi et al. (1998), is a signal pre-processing technique, used to restore coherence between data acquired before and after compression. It operates a 2D signal restoration at both global and local levels. However, the signal is only scaled during the global companding process, whereas signal shape modification inherently has a local character. The Lagrangian Speckle Model Estimator proposed by Maurice et al. (2004) is based on a linear tissue displacement model, whose parameters are estimated by minimizing an error criterion between pre- and post-compression regions. Yet, this estimator requires a preliminary stage to compensate for the 2D global

translation that occurs between the pre- and the post-compression regions of interest. The correlation techniques used for this step can be inaccurate in the case of highly strained regions and may therefore corrupt the strain estimation.

- (iii) Chen et al. (2004) proposed an original method to improve the estimation of lateral displacements. To enhance lateral tracking accuracy, the analytic signal spectrum is divided with respect to zero frequency in the lateral direction, in order to create a synthetic lateral phase. Phase-zero crossing is then locally performed in both dimensions to find the 2D displacement. However, this technique is only effective for low deformation regions (i.e., <1%). Liebgott et al. (2005) introduced a method to accurately estimate the axial and lateral components of the displacement using an original beam-forming scheme. The latter leads to the generation of images with oscillations in the lateral direction, which enables lateral tracking of the scatterers. Yet, this technique requires a specific ultrasound device dedicated to research applications.

However, 2D estimators may lead to noisy elastograms if significant out-of-plane motion occurs, since it is a source of decorrelation between pre- and post-compression signals. To overcome this decorrelation problem and accurately track the motion of the scatterers, the elevational movement must also be considered, requiring the acquisition of ultrasound RF volumes. The recent development of 2D (matrix-shaped) transducer arrays makes the acquisition of 3D data sets possible, thus exploiting the 3D speckle in the 3D space. Moreover, 3D strain estimators can provide all the components of the strain tensor. It is another advantage of 3D strain estimation, especially if strain estimation is the preliminary stage to solve the inverse problem of Young's modulus reconstruction.

However, very few 3D methods have been developed to date. Most of them originate from the 2D techniques previously detailed. Two-dimensional speckle tracking was indeed extended to the third dimension by Chen et al. (2005). Their 3D correlation-based speckle tracking algorithm therefore demonstrated the feasibility of 3D ultrasound elastography. But even if it outperforms 1D and 2D speckle tracking methods, the algorithm can be improved, since it does not consider any signal shape variation. The method originally developed by Konofagou and Ophir (1998) was adapted by Said et al. (2006) to process 3D sectorial data. However, this approach does not consider the 3D problem globally, but only a 1D movement in each of the three directions. The estimation accuracy also remains limited by the interpolation rate initially chosen. Techavipoo et al. (2004) developed a method using several angular insonifications. The displacement is calculated along each direction, and a least squares curve fitting algorithm estimates local tissue displacement. The authors show convincing results, but this technique requires a complex transducer beam-steering scheme based on multiple ultrasound insonification directions.

In this paper, we propose a 3D strain estimator that computes the axial strain while considering lateral and elevational motions. This 3D model is based on an adaptive and iterative constrained minimization strategy. The strain estimator is introduced in Section 2: the underlying mechanical and acoustical hypotheses used for our model are explained and the algorithm is described in detail. Section 3 discusses the results obtained for both simulated and experimental data. Section 4 provides concluding remarks and future perspectives.

## 2. Method

The estimator described in this section is based on the 2D model previously developed by our team (Brusseau et al., 2008), which has been adapted to consider the 3D tissue motion that occurs dur-

ing the static load. Its purpose is to accurately estimate the axial strain, while considering lateral and elevational motions.

With the static compression required to acquire the post-compression signals, the investigated tissues experience axial compression, but also lateral and elevational expansions. As a first approximation, we can consider that the related ultrasonic volume locally undergoes a similar transformation: 3D acoustical signatures are scaled – either stretched or compressed – in the three directions. Unfortunately, ultrasound data resolution is highly anisotropic. Owing to ultrasonic device characteristics, lateral and elevational resolutions are much lower than the axial resolution. This observation has led to the following assumption: in the axial direction, the post-compression volume is assumed to be a locally time-delayed and scaled replica of the pre-compression volume, whereas in the two other directions it is only considered as a locally shifted version of the original one (Fig. 1). Therefore, the volume transformation is described by four parameters, which must be estimated: an axial delay (denoted  $d$ ), an axial scaling factor ( $\alpha$ ), and a lateral and an elevational shift ( $\tau$  and  $\nu$ , respectively). The relation between pre- and post-compression volumes, denoted  $V_1$  and  $V_2$ , respectively, can thus locally be formalized by the following relation:

$$V_1(x, y, z) = V_2(\alpha \cdot x + d, y + \tau, z + \nu) \quad (1)$$

where  $V_1(x, y, z)$  is the signal amplitude at the  $(x, y, z)$  position,  $x$  being the axial,  $y$  the lateral, and  $z$  the elevational spatial variable. To achieve the parameter estimation, an adaptive and iterative constrained optimization process is proposed. It can be divided into three different steps:

- The first stage of the process is selecting the local region of interest (ROI) through an adaptive displacement.
- The second step is estimating the parameter itself. For each 3D ROI  $R_1$  selected in the pre-compression volume  $V_1$ , its deformed version  $R_2$  is sought in the post-compression volume  $V_2$  and the corresponding local strain is then estimated.
- The two previous steps are iterated until the entire ultrasound volume is covered. Strain maps are then computed and displayed during the third step.

### 2.1. Adaptive displacement of the region of study

Locally estimating the set of parameters first means selecting ROIs, in both the pre- and post-compression volumes. Let us denote  $V_1$  the pre-compression volume and  $R_1$  a local 3D ROI in  $V_1$ . Similarly,  $V_2$  is the post-compression volume and  $R_2$  the local ROI in  $V_2$ , corresponding to the same physical tissue region as

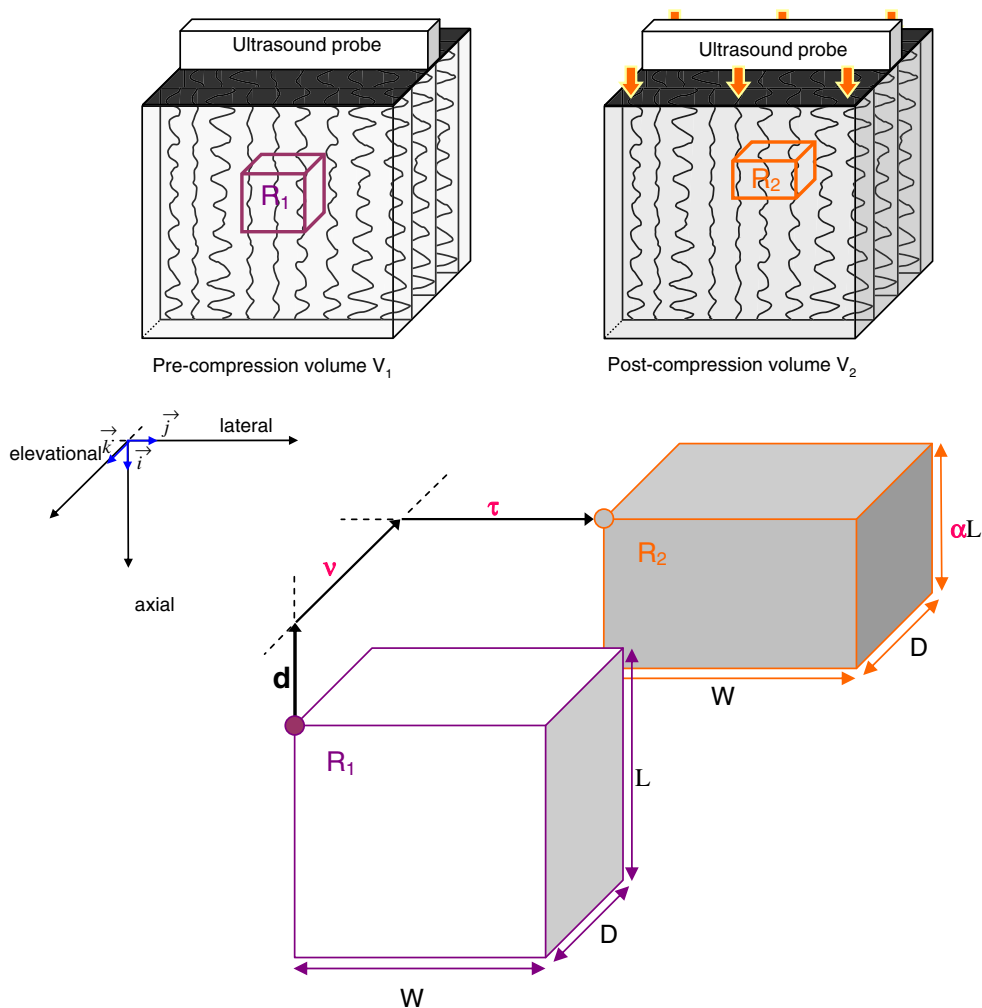


**Fig. 1.** Configuration of the acquisition.  $V_1$  and  $V_2$  denote the pre- and post-compression volumes, respectively. For each region of interest  $R_1$  selected in  $V_1$ , its deformed version  $R_2$  is sought in  $V_2$ , as an axially scaled and laterally and elevationally shifted replica of  $R_1$ .

the one inside  $R_1$ . In  $V_2$ , the position of  $R_2$  is different from that of  $R_1$  in  $V_1$ , owing to the deformation of surrounding regions involved in compression of the medium. To work with corresponding tissue regions,  $R_1$  and  $R_2$  are simultaneously and adaptively displaced. This tracks the motion of the scatterers better during compression, and therefore related ultrasound data can be considered in both volumes.

To cover the entire ultrasound volume  $V_1$ , the pre-compression 3D region of study  $R_1$  is regularly moved by constant steps of  $\Delta_{ax}$ ,  $\Delta_{lat}$ , and  $\Delta_{elev}$  in the axial, lateral, and elevational directions, respectively. Any overlaps can be considered to enhance the resolution of the final elastograms. More precisely,  $R_1$  is moved axially from the probe downward, laterally from the image center to the lateral boundaries, and elevationally from the image center to the elevational limits. Regarding the post-compression volume  $V_2$ , an adaptive displacement of the region of study  $R_2$  is considered.  $R_2$  axial displacement results from the accumulation of axial deformations of the regions located between the probe and the region of interest. The lateral and elevational displacements are directly linked to those estimated over adjacent regions. More formally, let us denote  $\mathcal{R}(O, \vec{i}, \vec{j}, \vec{k})$  the coordinate system,  $O$  being the center of the top surface of the ultrasound volume (Fig. 1). The positions of  $R_1$  in  $V_1$  and of  $R_2$  in  $V_2$ , denoted  $u_{R_1}$  and  $u_{R_2}$ , respectively, thus have the following expressions:

$$\text{Initialisation} \begin{cases} m_{u_{R_1}} = m_{u_{R_2}} = 0 \text{ if } m = 0 \\ n_{u_{R_1}} = n_{u_{R_2}} = 0 \text{ if } n = 0 \\ q_{u_{R_1}} = q_{u_{R_2}} = 0 \text{ if } q = 0 \end{cases} \quad (2)$$

$$\text{then} \begin{cases} u_{R_1}(m, n, q) = (m \cdot \Delta_{ax}, n \cdot \Delta_{lat}, q \cdot \Delta_{elev}) \\ u_{R_2}(m, n, q) = \left( \sum_{k=0}^{m-1} \alpha_k \cdot \Delta_{ax}, \sum_{k=0}^{n-1} \tau_k, \sum_{k=0}^{q-1} v_k \right) \text{ if } m, n, q \neq 0 \end{cases}$$

where  $\alpha_k$  is the axial scaling factor estimated for  $R_1$  at the position  $u_{R_1}(k, n, q)$ ,  $\tau_k$  the signed lateral displacement between  $R_1$  located at  $u_{R_1}(m, k, q)$  and  $R_2$  at  $u_{R_2}(m, k, q)$ , and  $v_k$  the signed elevational displacement between  $R_1$  at the position  $u_{R_1}(m, n, k)$  and  $R_2$  at  $u_{R_2}(m, n, k)$ . Consequently, the axial time-delay (parameter  $d$ ) between  $R_1$  and  $R_2$  is directly determined by estimating the axial scaling factors. At index  $m$ , the axial time-delay  $d_m$  is given by

$$d_m = m \cdot \Delta_{ax} - \sum_{k=0}^{m-1} \alpha_k \cdot \Delta_{ax} \quad (3)$$

and  $d_0 = 0$

Therefore, three parameters  $\alpha$ ,  $\tau$ , and  $v$  remain to be estimated. The two latter ones are of small magnitude, since the information of lateral and elevational shifts, previously estimated over surrounding regions, is progressively taken into account in the ROI adaptive displacement.

Once the positions of  $R_1$  in  $V_1$  and  $R_2$  in  $V_2$  are determined, the content of these two regions remain to be explicitly specified. Let  $L$  be the axial length,  $W$  the lateral width, and  $D$  the elevational depth.  $R_1$  positioned at  $u_{R_1}(m, n, q)$  is the part of  $V_1$  defined by

$$R_1 = V_1 \left( x, y, z \left/ \begin{cases} m \cdot \Delta_{ax} \leq x \leq m \cdot \Delta_{ax} + L - 1 \\ n \cdot \Delta_{lat} - \lfloor W/2 \rfloor \leq y \leq n \cdot \Delta_{lat} - \lfloor W/2 \rfloor + W - 1 \\ q \cdot \Delta_{elev} - \lfloor D/2 \rfloor \leq z \leq q \cdot \Delta_{elev} - \lfloor D/2 \rfloor + D - 1 \end{cases} \right. \right) \quad (4)$$

where  $\lfloor \cdot \rfloor$  represents the floor function.

A similar definition describes the post-compression region  $R_2$ .

## 2.2. Parameter joint estimation

Once the 3D regions of interest  $R_1$  and  $R_2$  are determined, the three parameters  $\alpha$ ,  $\tau$ , and  $v$  remain to be estimated. This step is achieved by optimizing a function, based on a similarity criterion between the two ROIs. The region of interest  $R_2$  is sought within  $V_2$ , as an axially scaled and laterally and elevationally shifted replica of  $R_1$ , denoted  $R_2(\alpha x, y + \tau, z + v)$ . The criterion chosen to evaluate the similarity between the ROIs is based on the normalized correlation coefficient. Since optimization problems are often formulated as the minimization of a function, we chose to minimize an objective function  $f$ , which is defined as the opposite of the normalized correlation coefficient between  $R_1$  and  $R_2$ , when  $R_2$  is compensated for the three parameters sought

$$f(\alpha, \tau, v) = \frac{- \sum_{x,y,z} \tilde{R}_1(x, y, z) \cdot \tilde{R}_2(\alpha x, y + \tau, z + v)}{\sqrt{\sum_{x,y,z} (\tilde{R}_1(x, y, z))^2} \cdot \sqrt{\sum_{x,y,z} (\tilde{R}_2(\alpha x, y + \tau, z + v))^2}} \quad (5)$$

where  $\tilde{R}_i(x, y, z) = R_i(x, y, z) - \bar{R}_i(x, y, z)$ , with  $\bar{R}_i(x, y, z)$  the mean value of signal amplitude over the region  $R_i$ .

In elastography, deformations induced by compression are of small magnitude (a few percent). Therefore  $R_2$  is sought in a small region immediately surrounding the position determined by  $u_{R_2}$ . Searching for a solution in a local neighborhood is equivalent to limiting the range of admissible values for the parameters  $\alpha$ ,  $\tau$ , and  $v$ . As a result, the optimization is subjected to a set of linear inequality constraints on the parameters. Since it drastically limits the possible occurrence of a local minimum for the objective function, these constraints contribute to improving the robustness of the algorithm. Reducing the parameter domain also speeds up the convergence process and saves calculation time.

The problem to be solved is therefore summarized by the following equation:

$$\begin{aligned} [\hat{\alpha}, \hat{\tau}, \hat{v}] &= \arg \min_{\alpha, \tau, v} f(\alpha, \tau, v) \\ \text{subjected to } &: \begin{cases} \alpha_{\min} \leq \alpha \leq \alpha_{\max}, \tau_{\min} \leq \tau \leq \tau_{\max}, v_{\min} \leq v \leq v_{\max} \end{cases} \end{aligned} \quad (6)$$

Adopting a matrix notation, the problem can be rewritten as

$$\begin{aligned} \hat{X} &= \arg \min_X f(X) \\ \text{subjected to } &: A \cdot X \leq b \end{aligned} \quad (7)$$

where  $X = [\alpha; \tau; v]$  is the parameter vector to be estimated,  $A$  is a coefficient matrix linked to the parameters, and  $b$  is a vector containing the bounds.

A feasible point  $X^*$  is a local minimum of (7) if

$$\begin{cases} A \cdot X^* \leq b \text{ with } \hat{A} \cdot X^* = \hat{b} \\ Z^T \cdot H(X^*) \cdot Z \text{ is positive semi-definite} \\ Z^T \cdot \nabla f(X^*) = 0 \iff \nabla f(X^*) + A^T \cdot \lambda^* = 0 \\ \lambda^* \geq 0 \\ \lambda_i^* \cdot (A_i \cdot X^* - b_i) = 0, \forall i \end{cases} \quad (8)$$

The three latter conditions define the Kuhn–Tucker conditions, used as the stop criterion of the iterative algorithm.  $\hat{A}$  is the submatrix of  $A$  containing the coefficients of the constraints active at  $X^*$  (those on bounds) and  $\hat{b}$  the subvector of  $b$ , such that  $\hat{A} \cdot X^* = \hat{b}$ .  $Z$  is the matrix whose columns form a basis for the set of vectors orthogonal to the rows of  $\hat{A}$ .  $\nabla f$  is the objective function gradient,  $Z^T \cdot \nabla f(X^*)$  and  $Z^T \cdot H(X^*) \cdot Z$  are the projected gradient and Hessian at  $X^*$ , respectively.  $\lambda^*$  is the vector containing the Lagrange multipliers  $\lambda_i^*$ .

The optimization algorithm is implemented as a sequential quadratic programming methodology (Boggs and Tolle, 1996), which models the defined problem at a given approximate solution by a quadratic programming subproblem. The current subproblem

solution is then iteratively used to construct a better approximation  $X_{k+1}$  according to the following scheme:

$$X_{k+1} = X_k + \rho_k \cdot d_k \quad (9)$$

where  $\rho_k$  is the descent step and  $d_k$  the descent direction, defined as the quadratic programming subproblem solution for the  $k$ th iteration. The quadratic programming subproblem is defined as

$$\min_{d_X} \nabla f(X_k)^T \cdot d_X + \frac{1}{2} d_X^T \cdot H(X_k) \cdot d_X \quad (10)$$

subjected to:  $A \cdot (d_X + X_k) \leq b$

where  $d_X = X - X_k$ ,  $\nabla f$  is the objective function gradient computed by a finite-difference approximation, and  $H$  is the Hessian of  $f$ . Since the calculation of  $H$  is a time-consuming procedure,  $H$  is initialized to the Identity matrix and a positive-definite approximation is iteratively built through BFGS updates (Gill et al., 1981). An active set strategy is used to find the solution  $d_X$  of the quadratic subproblem. This iterative procedure aims at identifying which inequality constraints will become active at the solution, determining the subspace  $Z$  of the feasible search directions. As  $Z_j$  is *a priori* not known, a typical iteration  $j$  consists in computing both a prediction  $Z_j$  of the subspace  $Z$  and the descent direction, following the scheme:

$$X_{j+1} = X_j + \zeta_j \cdot d_j \quad (11)$$

where the initial value of  $X_j$  corresponds to  $X_k$ , and where  $d_j = Z_j \cdot p$  is determined by solving the equation

$$\begin{aligned} (Z_j^T \cdot H \cdot Z_j) \cdot p &= -Z_j^T \cdot \nabla f_j \\ \text{with } \begin{cases} \nabla f_j &= \nabla f(X_0) + H \cdot (X_j - X_0) \\ X_{j=0} &= X_k \end{cases} \end{aligned} \quad (12)$$

The step length  $\zeta_j$  is either fixed to unity, if such a value is possible with no constraint violation, or is taken as the distance to the nearest constraint. When  $\zeta_j$  is equal to one, Lagrange multipliers are computed and if all positive, the quadratic programming minimum is achieved. Otherwise, if one or more multipliers are negative, the constraint associated with the most negative Lagrange multiplier is deleted from the active set,  $Z_j$  is updated and the process iterated. If  $\zeta_j$  is the distance to the nearest constraint, this blocking constraint is added to the active set,  $Z_j$  is updated, and a new iteration is performed. With the descent direction  $d_k$  established, the descent step  $\rho_k$  is computed to obtain a significant decrease in the objective function along the descent direction.  $\rho_k$  is restricted to the range  $[0; M]$ , where  $M$  is the distance to the nearest constraint along this direction  $d_k$ .

A new estimation is then computed, and the path to the final solution is constructed until the Kuhn–Tucker conditions are satisfied.

Sequential quadratic programming-based methods do not guarantee finding the global minimum of the objective function, but only a local solution. As previously mentioned, the parameter range is reduced to the admissible set

$$K = \left( \begin{bmatrix} \alpha \\ \tau \\ \nu \end{bmatrix} \in \mathfrak{R}^3 \middle/ \begin{cases} \alpha_{\min} \leq \alpha \leq \alpha_{\max} \\ \tau_{\min} \leq \tau \leq \tau_{\max} \\ \nu_{\min} \leq \nu \leq \nu_{\max} \end{cases} \right) \quad (13)$$

These powerful constraints associated with the optimization process are a first and simple way to reduce the possible occurrence of a local minimum, but they still do not prevent the algorithm from being trapped in a remote local minimum. Consequently, two additional procedures are implemented.

The first procedure aims at initializing the algorithm as close as possible to the global minimum. This is done by using the parameter vector solution information over surrounding regions as an

initial iterate for the optimization process. More precisely, the axial scaling factor is initialized to the mean value of the admissible range for the regions at the probe–medium interface and otherwise to the value previously obtained for the region immediately above the current position. Moreover, as the information from the lateral and elevational shifts estimated for surrounding regions is taken into account in the ROI adaptive displacement,  $\tau$  and  $\nu$  are expected to be of small magnitude. These two parameters are therefore initialized to zero.

A correction procedure is also implemented to improve the estimation reliability. This procedure is launched as soon as the estimation is considered unsatisfactory. To gauge the estimation quality, the normalized correlation coefficient value is considered. Indeed, the closer the correlation coefficient is to 1, the better the estimation. Specifically, when the correlation coefficient value is less than a threshold  $R_{\text{threshold}}$ , the correction procedure is started. An erroneous estimation may be caused by the convergence of the algorithm toward a local minimum because of an optimization initialization value that is too far from the solution. The algorithm is therefore reinitialized:  $N$  new minimization processes are launched from  $N$  initialization points uniformly spread within the admissible parameter domain  $K$ . Among these  $N$  new estimations, the one leading to the highest correlation coefficient is finally chosen.

### 2.3. Parameter field representation

Each position of  $R_1$  leads to an estimation of the parameter vector. Since  $R_1$  is regularly moved throughout the ultrasound volume  $V_1$ , the previous steps described in Sections 2.1 and 2.2 are repeated for each of its positions. The entire volume of ultrasound data is therefore covered, providing a volume of estimates for each parameter.

Our primary goal is to accurately represent the axial strain distribution inside the investigated volume, because this factor is the most significant for our application. The axial strain is directly linked to the estimated axial scaling factor  $\alpha_k$  according to the relation:

$$\hat{\epsilon}_k = \hat{\alpha}_k - 1. \quad (14)$$

Since our algorithm also evaluates lateral and elevational displacements, these distributions will also be presented.

Finally, the mean value of the normalized correlation coefficient over the ROI will also be considered, since it is an indication of the estimation's reliability. Indeed, a high correlation coefficient value means that the coherence between the pre- and post-compression signals has been restored with an adequate mechanical transformation. In this case, the parameter estimation is trustworthy.

## 3. Results

### 3.1. Results on simulated data

To assess the proposed 3D strain estimation algorithm, initial tests were run with simulated data.

Ultrasound elastography is designed for any medical application in which the development of a pathology involves local modifications in tissue stiffness. Since cancer detection will certainly become a common application in elastography, we chose to test our method on a numerical phantom mimicking the configuration of tumor tissue. This first phantom is designed as a  $30 \times 30 \times 30$ -mm<sup>3</sup> cube, within that is embedded a 10-mm-diameter spherical inclusion. The geometry of the phantom is further detailed in Fig. 2.

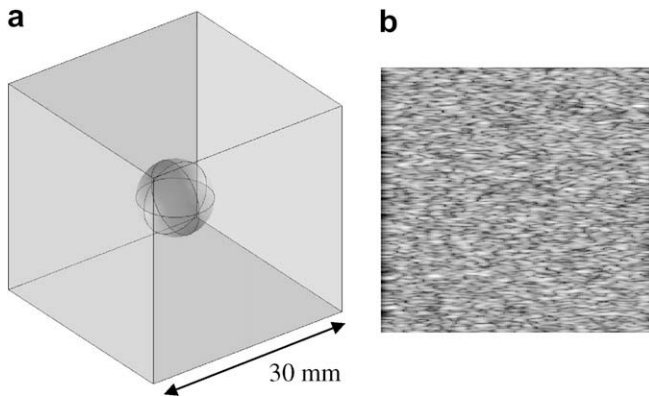


**Fig. 2.** (a) Geometry of the first numerical phantom. It is composed of two regions, a hard sphere ( $E = 90$  kPa) embedded in a softer background material ( $E = 30$  kPa). (b) A typical ultrasound image of one section of the first phantom.

The phantom properties were chosen considering two observations

- The pathological tissue's acoustical properties may exhibit no significant difference compared to the properties of healthy tissues, making them undetectable with a classical ultrasound scan.
- Pathological tissues such as tumors are stiffer than healthy tissues (Krouskop et al., 1998).

Therefore, the inclusion was designed to be three times stiffer than the surrounding medium, with a Young modulus of 90 kPa versus 30 kPa for the surrounding material. Such values are in agreement with those reported by Krouskop et al. (1998) for the breast elastic modulus, concerning the infiltrating carcinoma and the normal glandular tissue, respectively. Poisson's ratio was set at 0.49, both for the inclusion and the background.

The phantom was acoustically homogeneous (Fig. 2b), composed of a set of punctual scatterers, randomly positioned throughout the phantom volume on the basis of a uniform distribution. The number of scatterers in the entire volume is set to 3,000,000. Each scatterer was also assigned a back-scattering power, whose amplitude follows a normal distribution of zero-mean and with a standard deviation equal to 1. Regarding the B-mode image histogram, these settings led to a Rayleigh distribution of the grey level amplitude, which is the most common statistic for biological soft tissues (fully developed speckle).

The ultrasound RF volume was built by concatenating regularly spaced 2D scans, with the scan interdistance at 0.25 mm. The image formation was modeled as a linear space-invariant operation of convolution. First, the numerical phantom was elevationally divided into 0.25-mm-thick sections. Since each section was thin compared to the other dimensions (0.25 mm versus 30 mm), the section volume could be considered as negligible, and therefore scatterers were considered to be localized in a plane. Then the ultrasound image associated with a specific section was generated by convolving the acoustical scatterer distribution with the point spread function (PSF) of the ultrasound imaging system.

The chosen PSF was axially designed as a 7-MHz cosine function, modulated by a Gaussian function. Laterally, it was considered to be Gaussian-shaped. A slight curvature was also introduced to reproduce the shape of PSFs experimentally measured and provided in the literature (Du et al., 2006). The sampling frequency was set at 100 MHz and the sound speed was assumed to be 1540 m/s.

Forming the image for each section of the volume resulted in a set of elevationally regularly spaced 2D scans. The RF data volume was built by stacking the images.

Simulating the ultrasound post-compression volume required the calculation of the new positions of the scatterers in the phantom. The latter were determined through a finite element modeling (FEM). The phantom top surface was subjected to a 1.2-mm displacement along the axial axis, while the bottom surface was fixed along this direction, corresponding to a 4% uniaxial compression. Other boundaries were free to move. The FEM provided the scatterer displacements and therefore their new positions in the whole phantom. The latter were then used to calculate the ultrasound post-compression volume, as previously explained.

The data were finally composed of two RF ultrasound volumes (pre- and post-compression volumes), each of them having 4000 axial samples  $\times$  128 RF lines  $\times$  80 sections.

The ability of our algorithm to detect hard (pathological) areas was assessed on these data. Prior to strain computation, interpolation was performed with a factor 2 in the axial direction, in order to improve estimation accuracy. The size of the ROI  $R_1$  was 280 axial points  $\times$  four RF lines  $\times$  three elevational sections after this interpolation. This approximately represents a region of  $1 \times 0.9 \times 0.75$  mm<sup>3</sup>. Axial overlap was set at 80%, lateral overlap at 50%, and elevational overlap was equal to 66%. The parameter bounds were  $\alpha_{\min} = 0.94$  and  $\alpha_{\max} = 1$  for the axial scaling factor (which allows an axial strain in the range 0–6%),  $\tau_{\min} = -0.7$  mm and  $\tau_{\max} = 0.7$  mm for the lateral displacement ( $\pm 3$  RF lines),  $v_{\min} = -0.25$  mm and  $v_{\max} = 0.25$  mm for the elevational displacement ( $\pm 1$  section). Finally, the parameters  $R_{\text{threshold}}$  and  $N$  were set to 0.75 and 9, respectively.

The results are presented in Fig. 3. Although we are specifically interested in the axial strain distribution, in this section, lateral and elevational shift fields are also provided, in order to better assess the performance of our algorithm. Theoretical values for the axial strain, lateral displacement, and elevational motion are reported in Fig. 3a–c, respectively, whereas the corresponding estimated distributions are provided in Fig. 3d–f. We can first observe that all estimated parameter fields were very close to the theoretical values, with comparable progression and values. Whereas the inclusion was undetectable in the conventional B-mode scans (Fig. 2b), it was clearly delineated in the axial strain volume with sharp boundaries. More precisely, let us select a specific section, for instance the section at the elevational distance of 2.5 mm from the center (therefore crossing the inclusion, (Fig. 4)). It should be specified that a continuous progression has been observed between elevational sections. The estimated axial strain map (Fig. 4d) perfectly discriminates between the hard inclusion and the surrounding medium. The inclusion exhibits sharp boundaries, and the mean strain value over the healthy region is 1.9 times that of the tumor (4.1% versus 2.2%, respectively). Axial strain estimates are very close to the theoretical field (Fig. 4a).

Even if they are noisy because of the poor lateral resolution, the lateral displacement image (Fig. 4e) also agrees closely with theory (Fig. 4b). Because of the phantom configuration, out-of-plane motion was expected in this section. This can be observed on the estimated elevational displacement map (Fig. 4f), which is available with our technique. Compared to the theoretical field (Fig. 4c), this map shows the same pattern with a similar range of values. It is important to underline that elevational displacement is not uniform over the section considered: displacements up to 0.35 mm are reported, higher than the interdistance section. This observation validates our assumption that considering a 3D motion model is necessary. Moreover, even if this parameter alone could not discriminate the different areas, it interfered in the chosen deformation model. Therefore it contributes to improving both the quality and robustness of the estimation.

The advantage of considering the 3D motion of soft tissues was demonstrated anew when a comparison was made with a similar 2D estimator (no elevational displacement allowed, i.e.,  $v_{\min} = v_{\max} = 0$ ),

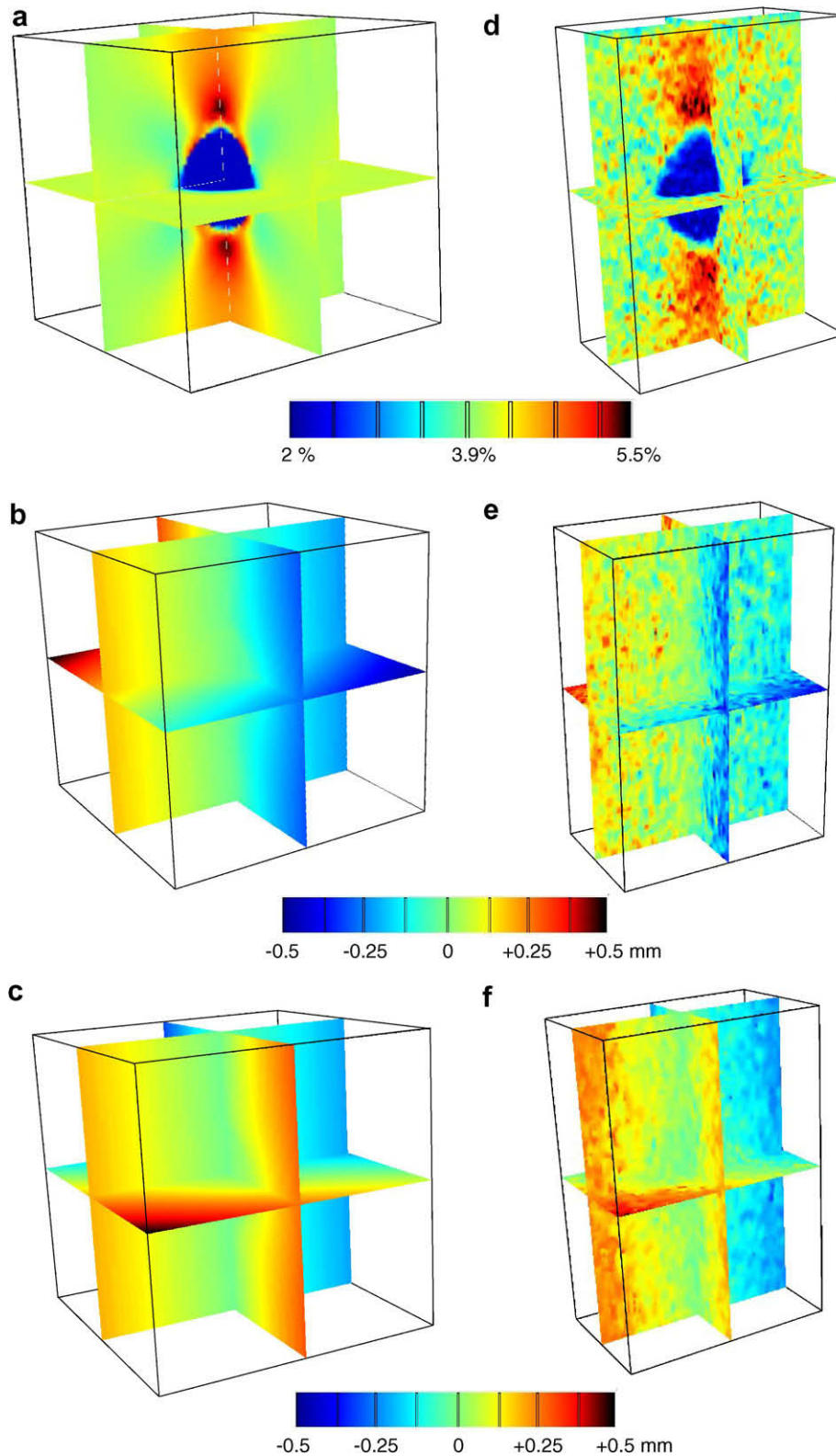


**Fig. 3.** Results from the cubic numerical phantom containing a hard spherical inclusion. Theoretical: (a) axial strain (in %), (b) lateral displacement (in mm), (c) elevational displacement (in mm) volumes. Estimated: (d) axial strains (in %), (e) lateral displacements (in mm) and (f) elevational displacements (in mm).

applied to the pair of pre- and post-compression images, both positioned at 2.5 mm from the center in the elevational direction (Fig. 4g). In the resulting axial strain image, erroneous estimated areas appear toward the lateral edges, because of significant out-of-plane motion over these regions.

Since the objective function of our algorithm was based on the normalized correlation coefficient (NCC), its mean value over the image was estimated at 0.79, which is a satisfactory value considering the complex configuration of the phantom and the poor resolution in the lateral and elevational directions.

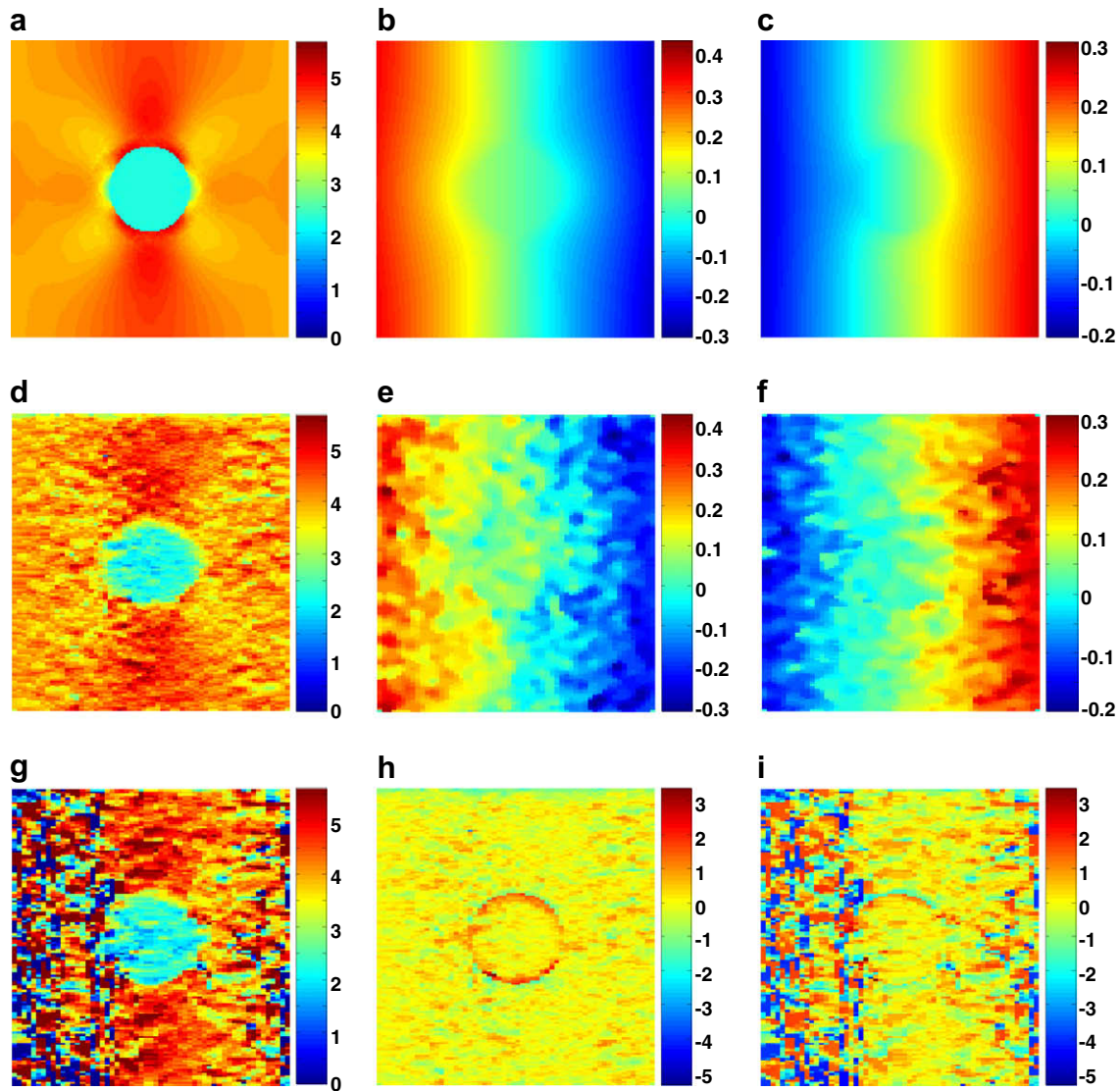


**Fig. 4.** Results obtained for one specific section, selected at 2.5 mm from the center in the elevational position. In the first row are the theoretical fields: (a) axial strain (in %), (b) lateral displacements (in mm) and (c) elevational displacements (in mm). In the second row are the fields estimated with the 3D algorithm: (d) axial strain (in %), (e) lateral displacements (in mm) and (f) elevational displacements (in mm). Third row: (g) axial strain with 2D algorithm, obtained by considering no out-of-plane motion (in %), (h) error map on the axial strain estimation with 3D algorithm and (i) with 2D algorithm (in %).

As a comparison, the NCC had a mean value of 0.64 in the 2D case.

To underline the improvement brought by the 3D estimator, axial strain error maps are also displayed, both for the 3D estimator and its 2D counterpart (Fig. 4h and i, respectively). These maps are computed as the signed difference between the estimated field and the theoretical one. The mean absolute errors for these images are 0.3% and 1% (3D and 2D, respectively), while the global compression of the phantom was 4%. For the 3D case, the largest errors are about 2% and they are found at the boundary between the inclusion and the surrounding tissue. This is due to the fact that the estimation is performed for a ROI positioned at the boundary between two regions of different mechanical behavior, while our algorithm assumes mechanical homogeneity for each specific ROI. Concerning the 2D case, error values go up to 5%. The largest errors are located on the sides of the image, because of out-of-plane motion.

A second numerical phantom was then considered, designed as a  $40 \times 40 \times 40$ -mm<sup>3</sup> cube, within that is embedded a 15-mm-diameter spherical inclusion. Its properties are the same as the

phantom previously described: Young's moduli of the inclusion and the surrounding material are 90 kPa and 30 kPa, respectively, Poisson's ratio is set to 0.49 and the phantom is acoustically homogeneous.

The deformation of the medium was calculated by a FEM, and was processed as if a probe was used to both compress the medium and acquire the data. In other words, the top surface of the phantom was not displaced uniformly downwards, but only the rectangular area corresponding to the probe surface was subjected to the compression (see Fig. 5m). Four different configurations were considered, depending on both the position of the probe and the static compression applied to the phantom. In a first case, the probe was located at the center of the phantom: the central plane of the phantom was therefore imaged. The probe was displaced downwards, either of 0.4 mm (1% global deformation) or 1.6 mm (4% deformation). A second configuration was proposed, where the probe was elevationally shifted of 5 mm, so that the insonified area did not cross the center plane of the phantom. The two levels of compression (1% and 4%) were still considered.

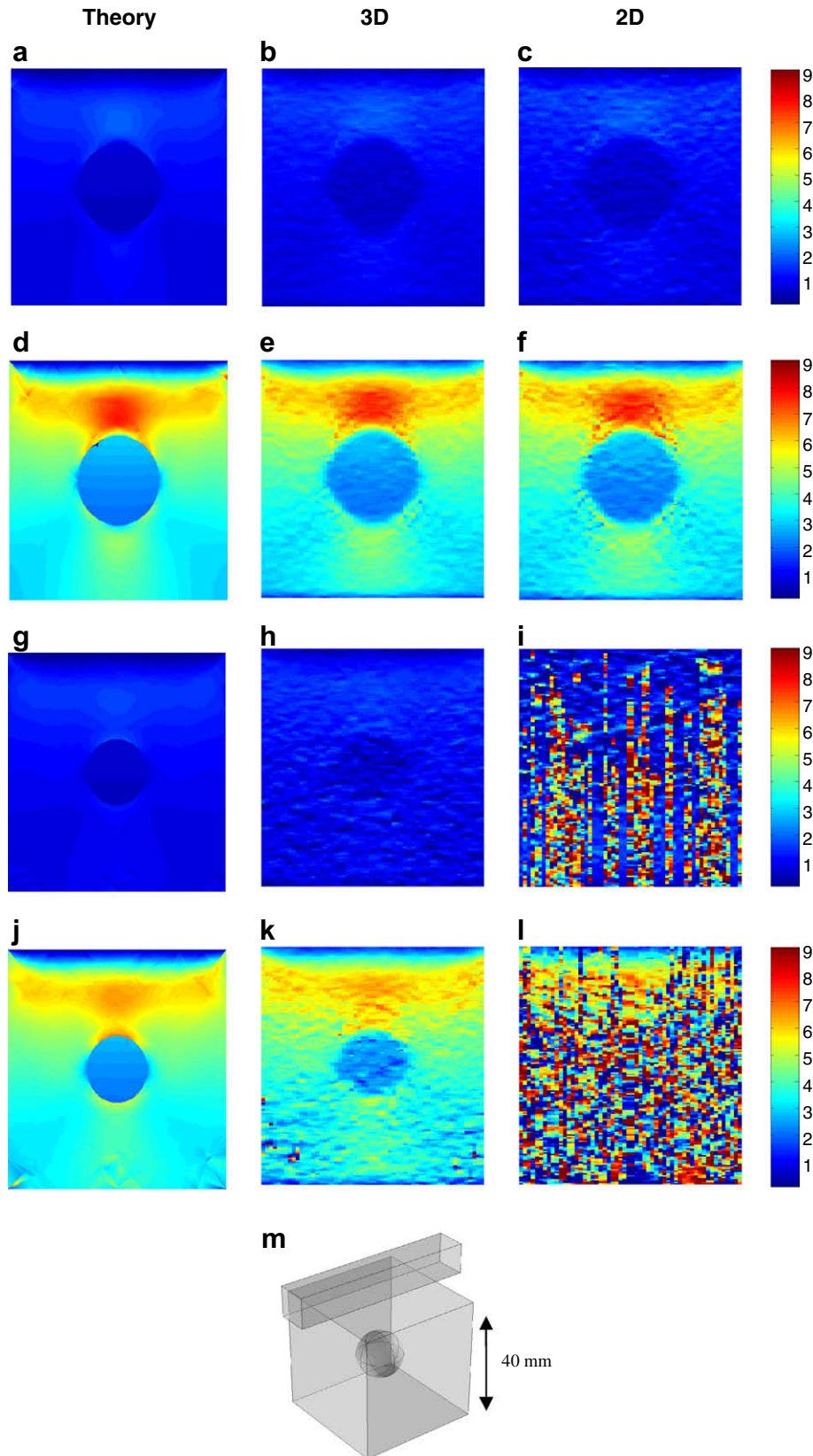


**Fig. 5.** Axial strain maps (in %) for the numerical phantom compressed by a probe. In the first column are the theoretical fields (FEM), in the second column are the results estimated with the 3D algorithm, and in the third column are the results estimated with the 2D algorithm. (a), (b), and (c) are the fields obtained for the middle section of the phantom and 1% deformation. (d), (e), and (f) are the fields for the middle section and 4% deformation. (g), (h), and (i) are the fields for the section at 5 mm of the center and 1% deformation. (j), (k), and (l) are the fields for the section at 5 mm and 4% deformation. (m) Geometry of the phantom.

The performances of the 3D algorithm and its 2D counterpart are compared in these four cases. Processing parameters are the same as those used for the first phantom.

Results are given (Fig. 5), with the same colorbar for all images. When the deformation is applied at the center of the phantom, 2D and 3D algorithms lead to similar results, and both estimations are very close to the theoretical fields, whatever the compression level (Fig. 5a–f). This can be explained by the fact that, owing to the symmetry of the phantom, out-of-plane motion in this section is almost zero. Indeed, elevational displacement values given by the FEM are in the range  $\pm 20 \mu\text{m}$ . The advantage of considering the third coordinate is in this particular case questionable. But as soon as the elevational motion is significant, 3D processing takes advantage over 2D. This can be seen in Fig. 5g–i. Even when a low compression is applied (1%), 2D tracking leads to numerous erroneous estimations, making the inclusion undetectable, whereas 3D algorithm yields estimations very close to the theoretical field. The relevance of the 3D algorithm versus 2D is emphasized when a higher compression is applied. 3D results are still close to the theory, and the inclusion is clearly visible with a 4% global compression (Fig. 5k).

These numerical experiments showed that the performances of 2D and 3D tracking are similar as long as out-of-plane motion is small. However, if significant out-of-plane displacements occur, the benefit of considering a 3D tracking is clearly demonstrated.

### 3.2. Results on experimental data

The ability of our method to process data acquired in clinical conditions was then assessed with a physical phantom made of polyvinyl alcohol (PVA) cryogel, which was designed to mimic an early-stage pressure ulcer.

A pressure ulcer is a pathology involving a hardening of damaged tissues (Gefen et al., 2005). This lesion is also deep within the body, making its detection at an early stage difficult. Elastography is a potential tool for detecting a developing pressure ulcer (Deprez et al., 2006).

PVA cryogel is a polymer that is now commonly used to build phantoms mimicking soft tissues. Mixed with Sigmacell particles, its acoustical properties are indeed very close to those of soft biological tissues, and this material is compatible with ultrasound imaging. Moreover, its stiffness increases with the number of freeze–thaw cycles applied. This typically covers a wide range of elasticity values, especially those commonly encountered for soft biological tissues (Fromageau et al., 2003).

Pressure ulcers are found on sites where thin-layer tissues are opposite a bony prominence. The phantom is therefore designed as a  $30 \times 60 \times 110\text{-mm}^3$  parallelepiped, with three distinct areas: a bone, a region mimicking the pressure ulcer at an early stage of the pathology, and surrounding healthy tissues. The geometry of the phantom is further detailed in Fig. 6. The bone, a forward limb of a dog, measures approximately 10 mm in diameter. The pathological area undergoes two freeze–thaw cycles, which is one more than the healthy region. This leads to a harder material for the area mimicking the pressure ulcer.

RF US data were acquired with an Ultrasonix Sonix RP device (Ultrasonix Medical Corporation, Richmond, BC, Canada). The probe and sampling frequencies were 7 MHz and 40 MHz, respectively. Each image was composed of 128 RF A-lines, with a 0.29-mm line interdistance. A linear stepper motor was used to move the probe elevationally, and regularly spaced 2D scans (by 0.2-mm steps) were acquired to cover the entire phantom volume. The pre-compression RF volume was thus obtained by stacking the set of 2D scans.

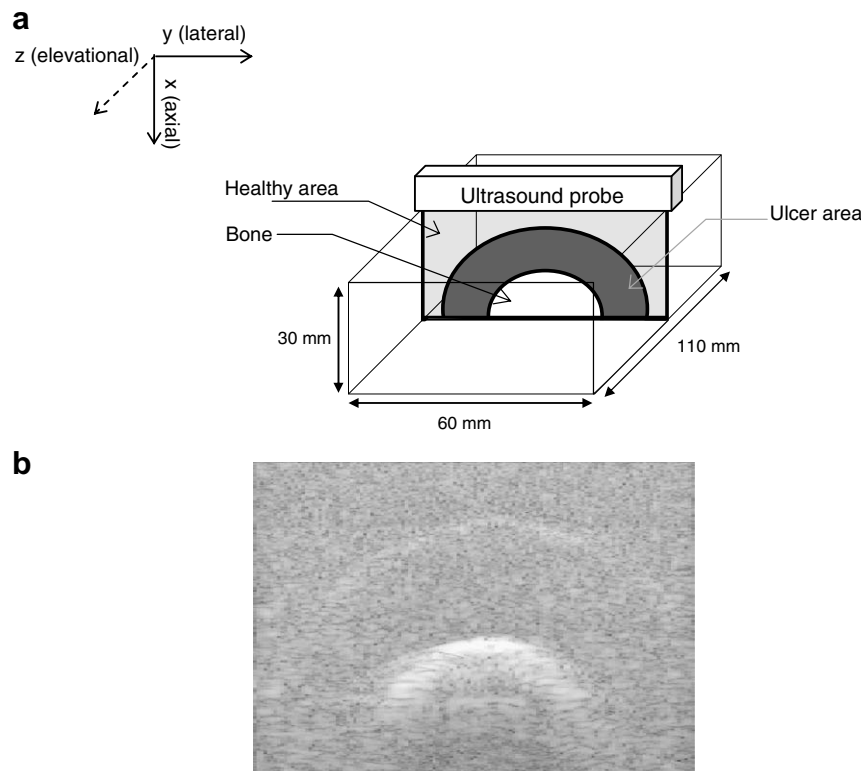


**Fig. 6.** (a) Scheme of the pressure ulcer-mimicking phantom. This physical phantom is composed of three regions, bone, the forward limb of a dog, healthy tissue, and pressure ulcer-mimicking areas made in PVA. The healthy region underwent one freeze–thaw cycle, whereas the diseased mimicking area had been subjected to two freeze–thaw cycles. (b) Typical ultrasound B-mode image of a section.

A thin plate was then used to uniformly compress the phantom. Since this plate is permeable to ultrasound, signals were acquired through the plate without any significant attenuation. The applied compression achieved a 2% global axial deformation. The same acquisition protocol as the one just detailed was applied anew to generate the post-compression volume.

The ability of our algorithm to deal with a real phantom was evaluated on these data. Prior to strain estimation, interpolation was performed with a factor of 5 and 2 in the axial and lateral directions, respectively. The size of the region of interest  $R_1$  was 300 axial points  $\times$  six RF lines  $\times$  three elevational sections. The overlap was set to 80%, both axially and laterally, and the elevational overlap was 33%.

The range of values allowed for the parameters were  $\alpha_{\min} = 0.92$  to  $\alpha_{\max} = 1$  for the axial scaling factor (representing an axial strain

up to 8%),  $\tau_{\min} = -0.85$  mm to  $\tau_{\max} = 0.85$  mm for the lateral displacement ( $\pm 6$  RF lines), and  $v_{\min} = -0.2$  mm to  $v_{\max} = 0.2$  mm for the elevational displacement ( $\pm 1$  section).  $R_{\text{threshold}}$  and  $N$  equaled 0.75 and 9, respectively.

The results are presented in Fig. 7. We can observe that the B-mode scan of the imaged area does not differentiate all structures (Fig. 6b). The bone is obviously hyperechoic, but the scan does not discriminate the hard and the soft areas except the interface, whereas these two regions are distinguishable in the axial strain map (Fig. 7a): the mean axial strain over the healthy (soft) region is approximately twice that of the pathological (hard) area, while the wall of the bone has a deformation almost equal to zero, as expected. Lateral and elevational displacement maps are also displayed (Fig. 7b and c). These maps remain noisy, mainly because of the poor resolution in these directions. But the border between

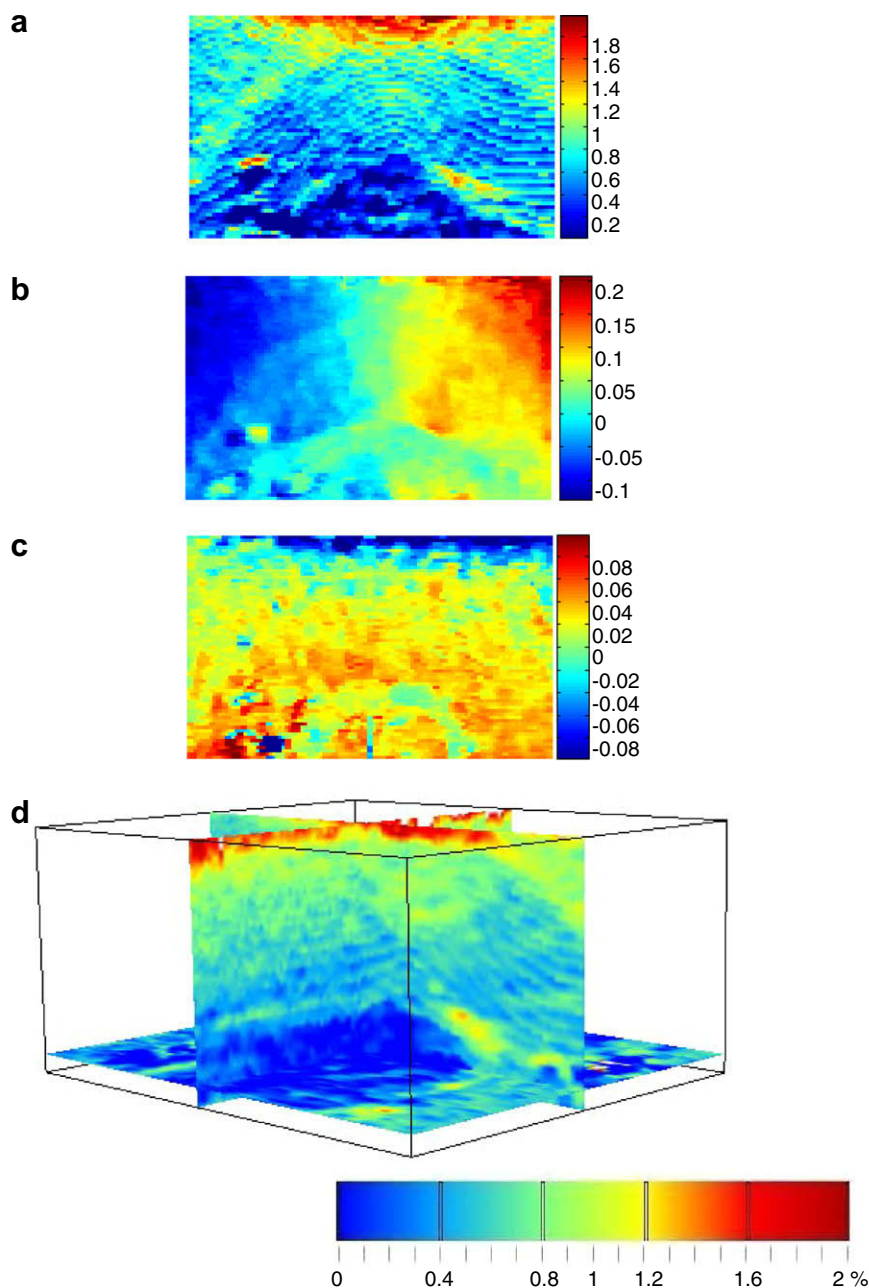


**Fig. 7.** Results from the physical phantom. Estimated: (a) axial strains (in %), (b) lateral displacements (in mm), and (c) elevational motions (in mm) for one specific section. (d) Estimated 3-D axial strain maps.

the two regions is visible on the lateral displacement map. For clinical purposes, identifying the border would be of great help in diagnosing the stage of the pathology. Surprisingly, the elevational map shows large displacements at the bone–cryogel interface. This might be attributable to a weak link between the bone and the cryogel, perhaps caused by the building procedure but also by their difference in nature, resulting in slippery conditions at this interface. However, this elevational parameter once again demonstrates the advantage of considering the 3D motion of soft tissues. This is confirmed by the associated normalized correlation coefficient map, where a high value was found throughout the chosen section using the 3D model. The mean value for this map was found to be 0.93.

As shown in the previous section, volume rendering can also be used to provide the radiologist with a better understanding of the medium's typology (Fig. 7d). Because of the low compression level applied to the phantom, strain values remained within a small range. Here again, the low resolution is a limitation. Yet, the three regions can be distinguished, since the deformation of the pathological area is approximately half the deformation of the surroundings.

The low contrast between the deformations of the two PVA layers can be explained by considering two assumptions. It could first be linked to the level of compression really applied to the phantom, which may have been smaller than 2%. A deformation of 2% corresponds to a small displacement of 0.6 mm. A minor error in the implementation of this displacement therefore leads to a more important change in the estimated strain. The low contrast could also be due to the material's properties themselves. It was indeed pointed out in the literature that the characteristics of PVA cryogel largely depend on several parameters, such as the sample volume, the chosen temperatures, the speed of decreasing and increasing temperature, or possible dehydration (Fromageau et al., 2007; Lozinsky et al., 2007). A single freeze–thaw cycle difference between the two regions might therefore lead to small changes in elasticity, as it can be expected for pressure ulcers.

#### 4. Conclusions

This paper has introduced a 3D strain estimation technique to image the deformation of soft biological tissues under load from the processing of RF ultrasound volumes. Contrary to other techniques modeling the compression-induced local displacements as translations, we have also considered a local scaling factor in the axial direction. Considering the modification in shape of the deformed data has provided estimation techniques that are more robust with regard to decorrelation noise. Optimal deformation parameters are locally estimated as those maximizing the normalized correlation coefficient between a 3D ROI and its deformed version, when the latter is compensated for these parameters.

Results on simulations and experimental data are very encouraging, demonstrating the ability of the proposed technique to provide good-quality 3D strain maps. Unlike 2D techniques, considering 3D tissue motion enables accurate estimations of the deformation even in the conditions of out-of-plane motion. For clinical purposes, the 3D visualization will be very helpful to provide physicians with a better understanding of the scanned area. With standard probes, clinicians access to the volume information by visualizing consecutive planes, requiring mental representation.

Future work will focus on decreasing the computational efforts of the algorithm. Indeed because of the 3D character of the model and the size of the data set, computing the elastogram for one section requires approximately 1 hour with a standard PC (2.6 GHz CPU and 1 Gb RAM) running with Matlab. Code optimization and parallel implementation will be considered.

#### References

- Alam, S.K., Ophir, J., Konofagou, E., 1998. An adaptive strain estimator for elastography. *IEEE Transactions on Ultrasonics, Ferroelectrics and Frequency Control* 45, 461–472.
- Anderson, W.A.D., Kissane, J.M., 1953. *Pathology*, ninth ed. C.V. Mosby Co., St. Louis.
- Ariel, I.M., Cleary, J.B., 1987. *Breast Cancer Diagnosis and Treatment*. McGraw-Hill, New York. p. 577.
- Bilgen, M., 1999. Wavelet-based strain estimator for elastography. *IEEE Transactions on Ultrasonics, Ferroelectrics and Frequency Control* 46 (6), 1407–1415.
- Boggs, P.T., Tolle, J.W., 1996. Sequential quadratic programming. *Acta Numerica* 4, 1–51.
- Brusseau, E., Perrey, C., Delachartre, P., Vogt, M., Vray, D., Ermert, H., 2000. Axial strain imaging using a local estimation of the scaling factor from RF ultrasound signals. *Ultrasonic Imaging* 22 (2), 95–107.
- Brusseau, E., Kybic, J., Deprez, J.F., Basset, O., 2008. 2D Locally regularized strain estimation algorithm: theoretical developments and results on experimental data. *IEEE Transactions on Medical Imaging* 27 (2), 145–160.
- Chaturvedi, P., Insana, M.F., Hall, T.J., 1998. 2D Companding for noise reduction in strain imaging. *IEEE Transactions on Ultrasonics, Ferroelectrics and Frequency Control* 45 (1), 179–191.
- Chen, X., Zohdy, M.J., Emilianov, S.Y., O'Donnell, M., 2004. Lateral speckle tracking using synthetic lateral phase. *IEEE Transactions on Ultrasonics, Ferroelectrics and Frequency Control* 51 (5), 540–550.
- Chen, X., Xie, H., Erkamp, R., Kim, K., Jia, C., Rubin, J.M., O'Donnell, M., 2005. 3-D Correlation-based speckle tracking. *Ultrasonic Imaging* 27, 21–36.
- Deprez, J.F., Brusseau, E., Gehin, C., Dittmar, A., Basset, O., 2006. 2D Elastographic technique dedicated to large lateral displacements: application to early detection of pressure ulcer. *IEEE Ultrasonics Symposium*.
- Du, H., Liu, J., Pellot Barakat, C., Insana, M.F., 2006. Optimizing multi-compression approaches to elasticity imaging. *IEEE Transactions on Ultrasonics, Ferroelectrics and Frequency Control* 53 (1), 90–99.
- Fromageau, J., Brusseau, E., Vray, D., Gimenez, G., Delachartre, P., 2003. Characterization of PVA cryogel for intravascular ultrasound elasticity imaging. *IEEE Transactions on Ultrasonics, Ferroelectrics and Frequency Control* 50 (10), 1324–1328.
- Fromageau, J., Gennisson, J.L., Schmitt, C., Maurice, R.L., Mongrain, R., Cloutier, G., 2007. Estimation of polyvinyl alcohol cryogel mechanical properties with four ultrasound elastography methods and comparison with gold standard testings. *IEEE Transactions on Ultrasonics, Ferroelectrics and Frequency Control* 54 (3), 498–509.
- Gefen, A., Gefen, N., Linder-Ganz, E., Margulies, S.S., 2005. In vivo muscle stiffening under bone compression promotes deep pressure sores. *Transactions of the ASME* 127 (June), 512–524.
- Gill, P.E., Murray, W., Wright, M.H., 1981. *Practical Optimization*. Academic Press, New-York. p. 388.
- Konofagou, E., Ophir, J., 1998. A new elastographic method for estimation and imaging of lateral displacements, lateral strains, corrected axial strains and poisson's ratios in tissues. *Ultrasound in Medicine and Biology* 24, 1183–1199.
- Krouskop, T.A., Wheeler, T.M., Kallel, F., Garra, B.S., Hall, T., 1998. Elastic moduli and prostate tissues under compression. *Ultrasonic Imaging* 20, 260–274.
- Lee, R.T., Grodzynsky, A.J., Frank, E.H., Kamm, R.D., Schoen, F.J., 1991. Structure-dependent dynamic mechanical behavior of fibrous caps from human atherosclerotic plaques. *Circulation* 83, 1764–1770.
- Lendon, C.L., Davies, M.J., Born, G.V., Richardson, P.D., 1991. Atherosclerotic plaque caps are locally weakened when macrophage density is increased. *Atherosclerosis* 87, 87–90.
- Liebgott, H., Fromageau, J., Wilhjelm, J.E., Vray, D., Delachartre, P., 2005. Beamforming scheme for 2D displacement estimation in ultrasound imaging. *EURASIP. Journal of Applied Signal Process* 8, 1212–1220.
- Lozinsky, V.I., Damshkaln, L.G., Shaskol'skii, B.L., Babushkina, T.A., Kurochkin, I.N., Kurochkin, I.I., 2007. Study of cryostructuring of polymer systems: 27. Physicochemical properties of poly(vinyl alcohol) cryogels and specific features of their macroporous morphology. *Colloid Journal* 69 (6), 747–764.
- Maurice, R.L., Ohayon, J., Frétygny, Y., Bertrand, M., Soulez, G., Cloutier, G., 2004. Noninvasive vascular elastography: theoretical framework. *IEEE Transactions on Medical Imaging* 23 (2), 164–180.
- O'Donnell, M., Skovoroda, A.R., Shapo, B.M., Emelianov, S.Y., 1994. Internal displacement and strain imaging using ultrasonic speckle tracking. *IEEE Transactions on Ultrasonics, Ferroelectrics and Frequency Control* 41 (3), 314–325.
- Ophir, J., Céspedes, I., Ponnekanti, H., Yazdi, Y., Li, X., 1991. Elastography: a quantitative method for imaging the elasticity of biological tissues. *Ultrasonic Imaging* 13, 111–134.
- Pellot-Barakat, C., Froin, F., Insana, M.F., Herment, A., 2004. Ultrasound elastography based on multiscale estimations of regularized displacement fields. *IEEE Transactions on Medical Imaging* 23 (2), 153–163.
- Said, G., Basset, O., Mari, J.M., Cachard, C., Brusseau, E., Vray, D., 2006. Experimental three dimensional strain estimation from ultrasonic sectorial data. *Ultrasonics* 44, 189–193.
- Techavipoo, U., Chen, Q., Varghese, T., Zagzebski, J.A., 2004. Estimation of displacement vectors and strain tensors in elastography using angular insonifications. *IEEE Transactions on Medical Imaging* 23 (12), 1479–1489.